Comparison and complementary use of in situ and remote sensing aerosol measurements in the Athens Metropolitan Area

S. Vratolis[☆,a,b], P. Fetfatzis[a], A. Argyrouli[g,h], O. Soupiona[b], M. Mylonaki[b], J. Maroufidis[b], A.-C. Kalogridis[a], M. Manousakas[a], S. Bezantakos[c], I. Binietoglou[i], L.D. Labzovskii[j], S. Solomos[m], A. Papayannis[b], G. Močnik[k,n], E. O' Connor[d,e], D. Müller[f], C.G. Tzanis[l], K. Eleftheriadis[a]

[a]*ERL, Institute of Nuclear & Radiological Sciences & Technology, Energy & Safety, National Centre of Scientific Research Demokritos, 15310 Ag. Paraskevi, Attiki, Greece*
[b]*Laser Remote Sensing Unit, Physics Department, School of Applied Mathematics and Physical Sciences, National Technical University of Athens (NTUA), 15780 Zografou, Greece*
[c]*Energy, Environment and Water Research Centre, The Cyprus Institute, Nicosia 2121 Cyprus*
[d]*Department of Meteorology, University of Reading, Reading, United Kingdom*
[e]*Finnish Meteorological Institute, Helsinki, Finland*
[f]*School of Physics, Astronomy and Mathematics, University of Hertfordshire, Herts AL 10 9AB, UK*
[g]*Technical University of Munich, TUM Department of Civil, Geo and Environmental Engineering, Chair of Remote Sensing Technology*
[h]*German Aerospace Centre (DLR), Remote Sensing Technology Institute, Oberpfaffenhofen, 82234, Wessling, Germany*
[i]*National Institute of Research and Development for Optoelectronics, Magurele, Romania*
[j]*Climate Research Division, National Institute of Meteorological Sciences (NIMS), Seogwipo, Jeju-Do, 63568, Republic of Korea*
[k]*Jožef Stefan Institute, Ljubljana 1000, Slovenia*
[l]*Climate and Climatic Change Group, Section of Environmental Physics and Meteorology, Department of Physics, National and Kapodistrian University of Athens, 15784 Athens, Greece*
[m]*Institute for Astronomy, Astrophysics, Space Applications and Remote Sensing, National Observatory of Athens, 15236, Athens, Greece*
[n]*University of Nova Gorica, 5000 Nova Gorica, Slovenia*

Abstract

In the summer of 2014 in situ and remote sensing instruments were deployed in Athens, in order to study the concentration, physical properties, and chemical composition of aerosols. In this manuscript we aim to combine the measurements of collocated in situ and remote sensing instruments by comparison and complementary use, in order to increase the accuracy of predictions concerning climate change and human health. We also develop a new method in order to select days when a direct comparison on in situ and remote sensing instruments is possible. On selected days that displayed significant turbulence up to approximately 1,000 m above ground level (agl), we acquired the aerosol extinction or scattering coefficient by in situ instruments using three approaches. In the first approach the aerosol extinction coefficient was acquired by adding a Nephelometer scattering coefficient in ambient conditions and an Aethalometer absorption coefficient. The correlation between the in situ and remote sensing instruments was good (coefficient of determination R^2 equal to 0.69). In the second approach we acquired the aerosol refractive index by fitting dry Nephelometer and Aethalometer measurements with Mie algorithm calculations of the scattering and absorption coefficients for the size distribution up to a maximum diameter of 1,000 nm obtained by in situ instruments. The correlation in this case was relatively good (R^2 equal to 0.56). Our next step was to compare the extinction coefficient acquired by remote sensing instruments to the scattering coefficient calculated by Mie algorithm using the size distribution up to a maximum diameter of 1,000 nm and the equivalent refractive index (ERI_{COR}), which is acquired by the comparison of the size distributions obtained by a Scanning Mobility Particle Sizer (SMPS) and an Optical Particle Counter (OPC). The agreement between the in situ and remote sensing instruments in this case was not satisfactory (R^2 equal to 0.35). The last comparison for the selected days was between the aerosol extinction Ångström exponent acquired by in situ and remote sensing instruments. The correlation was not satisfactory (R^2 equal to 0.4), probably due to differences in the number size distributions present in the air volumes measured by in situ and remote sensing instruments. We also present a day that a Saharan dust event occurred in Athens in order to demonstrate the information we obtain through the synergy of in situ and remote sensing instruments on how regional aerosol is added to local aerosol, especially during pollution events due to long range transport.

Keywords: Aerosol mixing in the vertical
In situ - Remote sensing comparison
Regional aerosol addition to local aerosol

[☆]Corresponding Author
Email address: vratolis@ipta.demokritos.gr (S. Vratolis)

1. Introduction

Human health, air quality, atmospheric visibility, and the climate are affected by aerosol particles (Fuzzi et al., 2015). In

order to understand these effects, measurements of atmospheric aerosol particle number size distribution, optical properties and chemical composition are highly needed.

Ground based in situ and remote sensing measurement platforms are crucial tools for continuous monitoring and evaluation of global, regional, and local air quality. In situ instruments provide extensive measurements of aerosol and trace gas chemistry (Lazaridis et al., 2006) as well as physical properties (Bryant et al., 2006) in the Mediterranean region. They also display excellent temporal resolution. Lidar observations provide the vertical profile of aerosol particle size distribution, their optical and physical properties (Sawamura et al., 2017).

Furthermore, measurements of vertical distributions of aerosol concentration, as well as the understanding of vertical mixing processes, provide an important input for understanding the dispersion of aerosols from local pollution sources and establish efficient control of air quality. Information about the depth and dynamics of the atmospheric boundary layer (BL) is essential to explaining in situ measurements of atmospheric species. In order to understand the processes that affect concentrations of species emitted within the surface layer, the knowledge of transport and mixing conditions including mean horizontal wind speed and direction profiles, strength of turbulence, and depth of the atmospheric BL is indispensable. The BL is defined here as the layer of atmosphere in turbulent connection with the surface of the earth. The height of the BL, referred to in this article as the mixing height (MH), defines the volume of atmosphere in which gas-phase or aerosol chemical species, emitted within the BL, are mixed and dispersed. Based on surface-level in situ measurements of aerosol properties and size distributions, knowledge about the height to which particles may be mixed can also improve assumptions about aerosol properties aloft for the purpose of aerosol-cloud interaction studies. The combination of MH, updrafts, wind speed and direction, and other meteorological information is essential to understanding of in situ atmospheric chemistry measurements made during air quality studies. Well-mixed BLs often occur over/near land in the unstable daytime convective boundary layer (CBL), typically as a result of surface heating. Stable boundary layer (SBL) conditions may be observed over land, typically at night where, in the absence of surface heating, the BL is in general not well mixed. SBL conditions are also observed over cold oceans. Very stable boundary layers (vSBL), typically observed over land, exhibit weak shear turbulence and strong temperature gradients near the surface (Tucker et al., 2009).

The aim of this work, in addition to reporting the aerosol measurements conducted, is to combine the measurements of collocated in situ and remote sensing instruments in order to increase the accuracy of predictions concerning climate change and human health. This combination can be achieved either by comparing or complementing. The results of the comparison will allow us to reduce the uncertainty of aerosol measurements in the atmosphere, subsequently improving model predictions on climate change. We also aim to find the atmospheric conditions that allow the direct comparison of in situ and remote sensing measurements. The results of complementing will give us insight regarding pollution dispersion in urban areas. Also, collocated in situ and remote sensing aerosol measurement stations, after this work, will be able to combine their measurements, so as to investigate the vertical mixing of aerosols and acquire a profile of aerosol properties extending from ground level to several km above ground level (agl). Thus, we will obtain an insight on how regional aerosol is added to local aerosol, especially during pollution events due to long range transport (Saharan dust, Biomass Burning, etc.). This knowledge, combined with lung deposition models, will allow us to predict the impact of aerosol particles (produced in the vicinity of the Athens Metropolitan Area (AMA) and transported from distant areas) on human health with higher accuracy. Therefore, using a combination of in situ instruments, remote sensing instruments and models, we could increase the quality of life for the people living in the AMA.

In order to achieve these goals, the optical properties of aerosol particles have to be estimated. To accomplish that we use Mie theory which gives an analytical solution of the Maxwell's equations for the scattering of electromagnetic radiation by spherical particles (Bohren and Huffman, 1998). The scattering phase function can be estimated for a specific aerosol radius and refractive index.

A key challenge in relating the remote sensing (Lidar) and in situ aerosol measurements is that the former are made under ambient Relative Humidity (RH) conditions, while the latter are made under dry RH conditions (typically $\leq 20\ \%RH$) (Zieger et al., 2011, 2012). At high RH, hygroscopic aerosols uptake water, which affects their optically relevant properties (e.g., size, morphology, and refractive index). The growth of an aerosol particle due to water uptake is described by the hygroscopic growth factor g(RH) which is defined as the particle diameter D_{wet} at a certain RH divided by its dry diameter D_{dry}:

$$g(RH) = \frac{D_{wet(RH)}}{D_{dry}}.$$

In order to address the influence of hygroscopic growth, we use two approaches: In the first approach we apply a scattering enhancement due to hygroscopic growth f(RH) factor to in situ data, while in the second approach we convert the dry aerosol size distribution measured in situ and the aerosol refractive index to ambient conditions using hygroscopicity κ acquired by a Hygroscopic Tandem Differential Mobility Analyzer (HT-DMA) measurements. In both cases, we compare these data to those obtained via multi-wavelength lidar measurements.

The Athens Metropolitan Area (AMA) is an ideal location to study these issues. It is densely populated and hosts many commercial and industrial activities in a relatively small area. High aerosol concentrations can be present during long periods of time (Vratolis et al., 2019). Strong vertical aerosol gradients in the lower troposphere can form in regions surrounded by mountains, under stable atmospheric conditions with weak air circulation and high anthropogenic activity (Wang et al., 2019).

In this study, in sections 2 and 3 we present the instrumentation and methods used. In section 4 we introduce the results we obtained, while in section 5 we present the summary and conclusions.
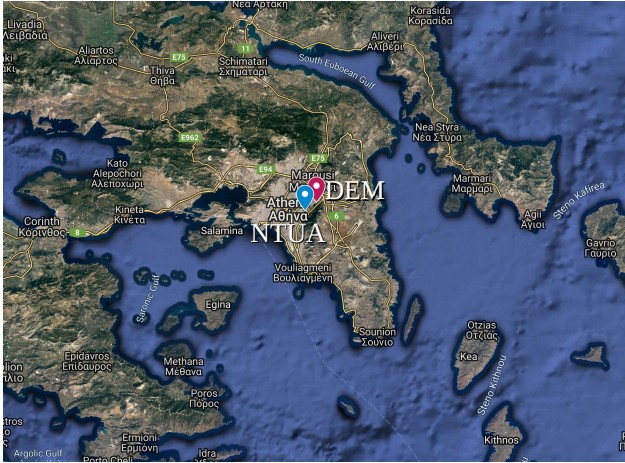
2

Figure 1: Major measurement sites in Attica (Greece) during the HygrA-CD campaign (Google, 2019).

2. Instrumentation

Hygroscopic Aerosols to Cloud Droplets (HygrA-CD) campaign was conducted in the Athens Metropolitan Area (AMA) from 15 May to 22 June 2014. It provided an extended record of data on aerosols and their role in cloud formation (Papayannis et al., 2017).

The campaign's major sampling site was the Demokritos station (DEM, red marker, Figure 1), member of the GAW and ACTRIS Networks (37.995° N 23.816° E, at 270 m above sea level (asl)). DEM station belongs to the National Centre of Scientific Research Demokritos, and it is situated in a pine forest, on the foot of Mount Hymettus, about 8 km to the north from Athens city center. It is an urban background station, representative of the atmospheric aerosol in the suburbs of the Athens Metropolitan Area. Katabatic winds influence the station frequently (Flocas et al., 1998), bringing air masses from Mount Hymettus (peak height 1,024 meters). An increase in particle number concentration during the night is occasionally observed, even in the absence of aerosol particle sources, due to the lowering of the nocturnal boundary layer height (NBLH).

The second campaign site was located at the National Technical University of Athens (NTUA, blue marker, Figure 1, 37.97° N, 23.79° E, 212 m asl), about 5 km to the north from downtown Athens.

2.1. In situ Aerosol Instruments

At DEM station, the following in situ aerosol instruments were operating during the campaign:

1. An Optical Particle Counter (OPC) (Grimm 107@660 nm laser light wavelength) to get the particle number size distribution for the sizes ranging from 250 nm to 2.5 μm (optical diameter). The OPC has participated in an intercomparison workshop at the WCCAP and exhibited a counting accuracy within 10% for the size range 250 nm to 1 μm. A measurement of the full size distribution is completed in 1 minute. The laser light used by the instrument emits electromagnetic radiation with a wavelength of 660

nm, while the light scattered by each aerosol particle is collected and measured for the angles 29.5°-150.5° and 81°-99° (Bukowiecki et al., 2011). Once manufactured, the instrument's 1 μm channel is electronically adjusted with 1 μm monodisperse polystyrene latex spheres (PSL) (Duke Scientific, NIST traceable, m = 1.59, according to ISO 21501-1) (Schneider, 2016; Grimm-Aerosoltechnik, 2005). Calibration to a reference Grimm OPC, using dolomite aerosols follows (i.e. dolomite has a different refractive index from PSL, and a full size distribution is used). The OPC particle number concentration in each size bin is adjusted to the measurements of the reference instrument by changing the detection limit thresholds for each size bin. (Lymperopoulos, 2015; Schneider, 2016; Grimm-Aerosoltechnik, 2005). The reference Grimm OPC is checked and certified with monodisperse polystyrene latex spheres (PSL) (Grimm-Aerosoltechnik, 2005). The OPC number size distribution acquired by the instrument was adjusted based on a calibration measurement with PSL spheres of 262 and 490 nm ((Vratolis et al., 2018), see supplementary material, Figures S14-S16).

2. An AE33 dual spot, seven wavelength (370, 470, 520, 590, 660, 880, 950 nm) Aethalometer to acquire the equivalent black carbon concentration (eBC). The instrument operated after a $PM_{2.5}$ inlet and completed an eBC measurement for all wavelengths every 1 minute. The aerosol absorption coefficient was acquired using a multiple scattering correction factor (C_0) equal to 3.5 in order to correct for multiple scattering by the filter fibers and the scattering of the aerosols embedded in the filter (Kalogridis et al., 2018). The instrument participated in an intercomparison workshop in 2017 at the WCCAP, exhibiting an equivalent Black Carbon (eBC) counting accuracy within 4% against a reference system (MAAP) under controlled laboratory conditions. Since the main light absorbing species is soot aerosol and this constituent is dominantly found withing the $PM_{2.5}$ size fraction, we do not expect that the inlet size cut will affect the results obtained in this work (Diapouli et al., 2017a).

3. A Scanning Mobility Particle Sizer (SMPS) to provide the particle number size distribution of atmospheric aerosol in the size range from 10 to 550 nm (electrical mobility diameter), comprised of a TSI Model 3080L electrostatic classifier (TSI Inc., Shoreview, MN, USA) and a condensation particle counter (CPC; TSI Model 3772, TSI Inc., Shoreview, MN, USA). The instrument yields a full size distribution in the above mentioned range every 5 minutes. Calibration against a reference SMPS system at the WCCAP (World Calibration Centre for Aerosol Physics) was conducted in 2013. The instrument participated in an intercomparison workshop in 2016 at the WCCAP, exhibiting a counting accuracy within 10% for the size range 30-550 nm against a reference system under controlled laboratory conditions (Wiedensohler et al., 2012). The SMPS is calibrated at DEM station with PSL spheres with a size of 200 nm.

4. An Ecotech Aurora3000 3-wavelength (450, 525 and 635

nm) Nephelometer, operating after a PM_{10} inlet, in order to acquire the aerosol scattering and backscattering coefficients (σ_{scat}, σ_{bscat}) (Pandolfi et al., 2018). Each measurement for all wavelengths has a duration of 1 minute. The instrument participated in an intercomparison workshop in 2016 at the WCCAP, exhibiting counting accuracy at 450 and 635 nm wavelength within 6% against a reference system (Aurora4000) under controlled laboratory conditions.

5. A Hygroscopic Tandem Differential Mobility Analyzer (HTDMA) in order to acquire the hygroscopicity κ of aerosol particles. The instrument consists of two Differential Mobility Analyzers (DMAs) for sizing particles in the fine aerosol range, a humidification system, and an Ultra-fine Condensation Particle Counter (Stolzenburg and Mc-Murry, 1991). Aerosol particles were initially dried and passed through a bipolar charger before entering the first DMA (DMA-1). The monodisperse aerosol flow downstream DMA-1 was then exposed to elevated RH conditions inside the humidifier. The second DMA (DMA-2), which was also operated with a sheath flow of elevated RH, and the UCPC were used for measuring the size distribution of the particles downstream the humidifier (Bezantakos et al., 2013).

6. A high resolution energy dispersive, polarization geometry, X-Ray fluorescence spectrometer (XRF, model Epsilon 5 by PANanalytical) to measure the metal content of aerosol particles collected on $PM_{2.5}$ filters. The instrument has a Cartesian-triaxial geometry. 8 secondary targets (Al, CaF_2, Fe, Ge, Zr, Mo, Al_2O_3, LaB_6) are provided by the instrument, so as to polarize the X ray tube generated incident radiation. The sample heating and the Xray damage are kept minimum because of the combination of the low power and polarized optics that the instrument uses. PM samples can be measured repeatedly without sustaining any damage. (Manousakas et al., 2017).

Inlet aerosol flows are dried to RH below 40%, while particle losses due to diffusion in the pipe lines are calculated and corrected for SMPS. Other losses are not corrected for in situ instruments, as their inlet lines are vertical and therefore losses are not significant.

2.2. Remote Sensing Aerosol Instruments

A Doppler wind lidar system manufactured by HALO Photonics with a laser at 1.5 μm was operated at the DEM site by the Finnish Meteorological Institute (FMI). The instrument measurements used in the current study were those in the 3-beam Doppler beam swinging (DBS) mode. This Doppler beam swinging, or DBS technique is fast and simple both in the hardware and in the data evaluation algorithm, but lacks the goodness-of-fit information as a measure for the reliability of the results. This shortcoming is partially compensated by information about the temporal behavior of the data. Turbulence is easily determined from these data for any time scale as dictated by the particular process investigated, particularly as turbulence depends critically on ground roughness length and atmospheric stratification stability (Weitkamp, 2005). The vertical profiles of the radial Doppler wind velocity and 2-3D wind fields were acquired by the instrument, in addition to the atmospheric turbulent properties (e.g. turbulent dissipation rate, ϵ) (O'Connor et al., 2010). The wind velocity is provided with accuracy better than 0.5 ms^{-1} for DBS mode. The vertical resolution of the measurements is 30 m, and the temporal resolution is 14 seconds for DBS mode. The maximum range achieved is 2-3 km depending on the atmospheric aerosol load, but it could reach 10 km height, under the presence of clouds (Papayannis et al., 2017).

The remote sensing instruments that were in operation at NTUA station during the campaign included:

1. The EOLE Raman lidar system. Its laser source is a pulsed solid state Nd:YAG (Neodymium-doped Yttrium Aluminium Garnet) laser. The primary laser beam is emitted at 1064 nm with 10 Hz repetition frequency. The energy of each laser pulse is, at the beginning, 850 mJ. The second and third harmonic frequencies of the Nd:YAG system (at 532 nm and 355 nm, respectively) are generated with the use of two non-linear KD*P (Potassium Dideuterium Phosphate) crystals (Argyrouli, 2016). The backscattered signal is measured at 355, 532 and 1064 nm and the Raman signal is measured at 387, 407 and 607 nm. The instrument provided the vertical profiles of the aerosol backscatter coefficient (b_{aer}) (355, 532 and 1064 nm) and aerosol extinction coefficient (a_{aer}) (355 and 532 nm), the aerosol Ångström exponent (AE) for b_{aer}, a_{aer}, and the lidar ratio ($S = a_{aer}/b_{aer}$) (at 355 and 532 nm). During nightie measurements, the profiles in the vertical of b_{aer}, a_{aer}, S, and AE for extinction and backscatter coefficients are obtained with 10 - 20%, 10 - 15%, 10% and 25% uncertainty, respectively (Kokkalis et al., 2012). During daytime measurements, by using as input a constant S value, we retrieve the b_{aer} and the AE-related to backscatter coefficient values with an average uncertainty of 20 - 30% and 25%, respectively (Kokkalis et al., 2012). The water vapor mixing ratio vertical profiles were also retrieved from 0.5 to 6-7 km height, during nighttime. The statistical error was $\geq$ than 8% at heights up to 2 km and ranged between 10 to 15% from 2.5 to 6 km (Mamouri et al., 2007). The measurements of b_{aer}, a_{aer} above the height of 1,200 m above sea level (asl) were considered meaningful and the average from 1,200 m asl to 1,300 m asl was used for the comparison to the in situ instruments.

2. A microwave radiometer (RPG-HATPRO model, RPG Radiometer Physics), operated at NTUA, provided temperature, Absolute Humidity (AH) and RH vertical profiles (Labzovskii et al., 2018). The root-mean-square (rms) accuracy of temperature was 0.6 K near the surface and it increased to 1.5 - 2.0 K in the middle troposphere (Crewell et al., 2001; Liljegren et al., 2005), while the rms of absolute humidity was 0.4 gm^{-3}. The integrated water vapour (IWV) and the liquid water path (LWP) retrievals had accuracies of 0.3 - 1.0 kgm^{-1} and 20 - 30 gm^{-2}, respectively (Loehnert and Crewell, 2003).

Radiosondes were also launched from the Hellenic National

4

Table 1: Instrument in brief, I.S. refers to in situ instruments, while R.S. refers to remote sensing instruments.

Instrument	Station	Quantity	Category
OPC	DEM	Size Distribution 0.25-2.5 μm	I.S.
AE33	DEM	eBC	I.S.
SMPS	DEM	Size Distribution 10-500 nm	I.S.
Aurora3000	DEM	σ_{scat}, σ_{bscat}	I.S.
HTDMA	DEM	κ	I.S.
XRF	DEM	$PM_{2.5}$ metal content	I.S.
HALO	DEM	ϵ	R.S.
EOLE	NTUA	a_{aer}, b_{aer}	R.S.
RPG-HATPRO	NTUA	RH	R.S.

Meteorological Service (HNMS, 37.88° N 23.73° E, at 10 m above sea level (asl)) or the National and Kapodistrian University of Athens (NKUA, 37.98° N 23.73° E, at 280 m above sea level (asl)) sites in Athens. The model of the radiosonde used was RS92-SGP, Vaisala Oyj. It provided the vertical profiles of temperature (uncertainty between 0.3 and 0.4 °C), RH (uncertainty 4%), pressure (uncertainty between 0.5 and 1 hPa for pressures ≥ 100 hPa) and wind speed and direction (uncertainties of 0.15 ms^{-1} and 2°, respectively) according to Nash et al. (2011) and Vaisala (2013a,b).

3. Methods

3.1. Choice of dry aerosol particle number size distribution extent

The aerosol dry size distribution used in the comparison of in situ and remote sensing instruments is obtained during the procedure in order to acquire the Equivalent Refractive Index (ERI_{COR}) optimal solution by fitting the SMPS and OPC size distributions in the overlapping range (Vratolis et al., 2018). Since the OPC number size distribution was corrected based on calibration measurements with PSL spheres with a diameter of 262 and 490 nm (see supplementary material, Figures S17-S19), we used the combined size distribution up to a maximum diameter of 1,000 nm (corresponds to dry electrical mobility diameter). After this size, we cannot be sure that ERI_{COR} corresponds to the aerosol particle's refractive index. Also, according to Heim et al. (2008), the OPC counting accuracy is within 10% of the ideal 100% for sizes from 0.3 to 1 μm (electrical mobility diameter). From around 0.8 μm up to 2 μm the sizing accuracy decreases. The obtained combined size distribution up to a maximum diameter of 1,000 nm from the SMPS and OPC (considered to correspond to electrical mobility diameter) is used from now on as the aerosol size distribution whose optical properties are compared to the EOLE lidar measurements. The counting accuracy of the SMPS in the size range 30 - 550

nm is 10%, therefore we expect the error in the size distribution produced by the combination and adjustment of SMPS and OPC measurements to be within an uncertainty of 10%. Furthermore, we expect the uncertainty of all comparisons presented in this work to be within 20%.

3.2. $RI_{AE33-NEPH}$ optimal solution algorithm

The Root Mean Square Error (RMSE) of the difference between the aerosol scattering and absorption coefficients measured by the Nephelometer ($Scat_{NEPH}$) and AE33 (Abs_{AE33}), and the scattering ($Scat_{NSD}$) and absorption (Abs_{NSD}) coefficients calculated using Mie theory for the combined size distribution of SMSP and OPC up to a maximum diameter of 1,000 nm (NSD) is produced according to equation 1:

$$\text{RMSE} = \left([Scat_{NEPH} - Scat_{NSD}]^2 + [Abs_{AE33} - Abs_{NSD}]^2 \right)^{0.5} \quad (1)$$

The $RI_{AE33-NEPH}$ optimal solution is obtained when we acquire the minimum RMSE in a fitting procedure where the aerosol refractive index is the independent variable. The resulting complex refractive index may be used to calculate the absorption and scattering coefficients at specific angles (i.e. backscattering), keeping in mind that we refer to spherical particles, as we use Mie algorithm.

3.3. Truncation error correction and calculation of the scattering coefficient for ambient conditions

The Nephelometer measurements are corrected for truncation errors following (Müller et al., 2011), while the scattering AE is used to adjust the scattering coefficient to 660 nm. In order to calculate the ambient scattering coefficient so as to compare to EOLE lidar extinction coefficient, the aerosol hygroscopic exponent γ was used (Gassó et al., 2000). The ambient RH is computed using the microwave radiometer measurements. The ambient aerosol scattering coefficient $\sigma_{scat,amb}$, at RH_{amb} is determined as

$$\sigma_{scat,amb} = \sigma_{scat,dry} \left(\frac{100 - RH_{dry}}{100 - RH_{amb}} \right)^{\gamma} \quad (2)$$

3.4. Refractive index and particle number size distribution in ambient conditions

The aerosol ERI_{COR} and $RI_{AE33-NEPH}$ were adjusted to ambient conditions, using the hygroscopicity κ acquired by the HTDMA measurements for a dry particle electrical mobility diameter equal to 250 nm. We computed the aerosol density according to Hasan and Dzubay (1983) using Equation 3:

$$\rho^{-1} = \sum_i \frac{X_i}{\rho_i} \quad (3)$$

where X_i and ρ_i are the mass fraction and density in gcm^{-3} for species i. Species 1 refers to the dry aerosol size distribution up to a maximum diameter of 1,000 nm with a refractive

index equal to ERI_{COR} or $RI_{AE33-NEPH}$ and a density equal to 1.48 gcm^{-3} (Gini et al., 2019). Species 2 refers to water. There are different mixing rules that could be applied in order to acquire the refractive index. The most common are partial molar refraction (Stelson, 1990) and the volume-weighted method (Hasan and Dzubay, 1983).

We used the volume-weighted method (Equation 4) so as to calculate the mean refractive index ($m = m_r - k_i$).

$$m = \rho \sum_i \frac{X_i m_{r,i}}{\rho_i} - \rho \sum_i \frac{X_i k_i}{\rho_i} i \qquad (4)$$

where m_r is the real part of a complex refractive index for species i and k_i is the imaginary part.

The particle number size distribution acquired by in situ instruments in dry conditions is also adjusted to ambient conditions based on the hygroscopicity κ and the ambient RH (microwave radiometer measurements).

3.5. Flexible Particle Dispersion Model (FLEXPART)

The Flexible Particle Dispersion Model (FLEXPART) was used to find the possible aerosol source areas of the measured atmospheric volume. To do this, FLEXPART simulates the backward trajectories of a large number of air parcels and estimates their residence time over each geographic grid cell (sensitivity) (Stohl and Thomson, 1999; Stohl et al., 2005). These residence times indicate how sensitive the measurements at a station are to emissions occurring at each geographic grid cell. FLEXPART takes into account not only grid scale wind but also turbulent and mesoscale wind fluctuations. Drift correction, in order to disallow accumulation of the released air parcels, and density correction, so as to take into account the decrease of air density with height, were both applied. We produced seven-day backward runs for the campaign period with the release of 4×10^4 computational air parcels every 3 hours beginning from DEM station. Thus, we acquired the residence times of these computational air parcels in each geographic grid cell, for a height from 0 to 100 m agl.

3.6. Richardson number derivation

The atmospheric conditions (including Richardson number) were analyzed by WRF-ARW model (Skamarock et al., 2005). The model covers three domains, namely Europe, Greece, and Athens. The external grid is at (12×12 km), while the two nested grids are at (4×4 km) and (1×1 km) respectively. The NCEP final analysis (FNL) and sea surface temperature (SST) are used for initial and boundary conditions (Solomos et al., 2019).

3.7. Segmentation algorithm for aerosol layers in atmospheric Lidar measurements

The detection-segmentation algorithm is based on image processing techniques. The algorithm takes as input the raw lidar data and produces a layer-labeled image. It is optical property independent and handles the lidar profiles (height over time) as 2D gray-scale images. First, a pre-processing is carried out to correct any noise and distortion. Then, the detection part extracts the useful lidar signal (aerosol/cloud layers) by using image thresholding techniques. Lastly, the segmentation is based on the watershed algorithm and the histogram-based classification Multi-Otsus method (Maroufidis et al., 2020).

3.8. Aerosol mineral dust concentration estimation based on XRF measurements

The estimation is based on XRF measurements and according to Nava et al. (2012):

$$\begin{aligned} \text{Mineral Dust} = {} & 1.35\, Na + 1.66\, Mg + 1.89 Al + 2.14\, Si \\ & + 1.21\, K + 1.40\, Ca + 1.67\, Ti + 1.43\, Fe \end{aligned} \quad (5)$$

We applied corrections in order to account for sea-salt contributions to Na and Mg. We calculated the sea salt fractions of Na and Mg using the measured Cl concentration. The sea salt ratios used for Na/Cl and Mg/Cl were 0.56 and 0.07, respectively. The drawback of this approach is that an overestimation of the non-sea salt component of Na and Mg is possible, as Cl may evaporate from the filters on which the aerosol samples are collected.

3.9. Method used in order to distinguish days that in situ and remote sensing instruments can be compared

In order to distinguish days that in situ and remote sensing instruments can be compared, we have to make sure that a well mixed boundary layer up to a height of 1,300 m asl is present. To do that, we apply the following three step method: In the first step, we visually inspect the atmospheric layers determined using image processing of the raw lidar data (method presented in section 3.7) and subsequently select days that have a layer extending from ground level to 1,300 m asl in the late afternoon - early evening. We are interested in this time period because the sun radiation intensity is low, resulting in more accurate extinction and backscattering coefficient determination by EOLE lidar, while the boundary layer is still deep. In the second step, we make sure that for the time periods selected earlier, the WRF Richardson number up to 1300 m asl is higher than 0.39, indicating that we are within the BLH. This threshold was selected according to Zhang et al. (2014). In the third step, we make sure that for the selected days there is significant turbulence in the atmosphere during noon, late afternoon, and early evening (ϵ values higher than 10^{-4} for a height extending from ground level up to 1,300 m asl). All days that do not fulfill these criteria cannot be compared.

4. Results and Discussion

4.1. Comparison of Nephelometer to ERI calculated total scattering coefficient

In Figure 2 we present the comparison of the scattering coefficient measured by Ecotech Nephelometer (adjusted to 660 nm wavelength, $Neph_{660}$) to the scattering coefficient ($SD -$
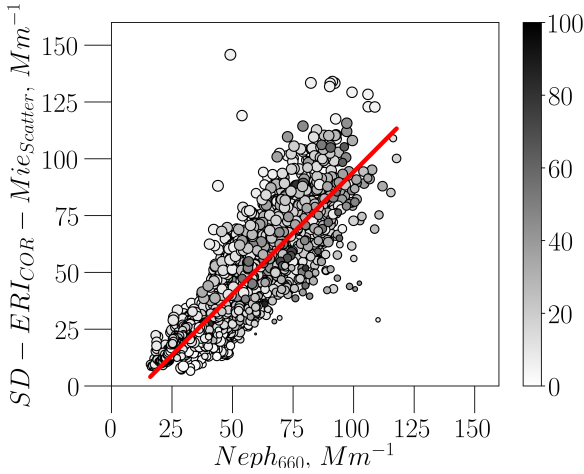
Figure 2: Comparison of the dry scattering coefficient $\sigma_{scat,dry}$ obtained by Mie algorithm calculation using ERI_{COR}, for sizes up to 1,000 nm (electrical mobility diameter), and the dry scattering coefficient obtained by Ecotech Nephelometer adjusted to 660 nm wavelength, corresponding to OPC. The color of the marker corresponds to the absorption coefficient measured by AE33, normalized between 0 and 100. The minimum value of the AE33 absorption depicted is 0.3 Mm^{-1} and the maximum value is 16 Mm^{-1}. The area of each marker corresponds to ERI_{COR}, normalized between 0 and 100. The maximum value of ERI_{COR} depicted is 1.7 and the minimum is 1.43. The red line depicts the relation of $SD - ERI_{COR} - Mie_{Scatter} = 1.07 * Neph_{660}$-13 Mm^{-1}, which is the best linear fit obtained, with a coefficient of determination (R^2) equal to 0.72.

$ERI_{COR} - Mie_{Scatter}$) obtained by the application of Mie algorithm on the unified aerosol size distribution (SD) of the instruments SMPS and OPC acquired in the process of defining ERI_{COR} (Vratolis et al., 2018). The refractive index used was ERI_{COR}. If we apply a linear fit, $SD - ERI_{COR} - Mie_{Scatter}$ equals 1.07 * $Neph_{660}$-13 Mm^{-1} with a coefficient of determination (R^2) equal to 0.72. $SD - ERI_{COR} - Mie_{Scatter}$ values are almost the same to those of the dry Nephelometer scattering coefficient, and there is a reasonably good agreement between the two quantities. This is an indication that the portion of the size distribution up to a maximum diameter of 1,000 nm can be used in order to compare optical properties of aerosols from in situ and remote sensing instruments. Keeping in mind the uncertainties in the size distribution measurements of SMPS, OPC and the uncertainty of ERI_{COR}, we expect the uncertainty in the estimation of $SD - ERI_{COR} - Mie_{Scatter}$ to be within 20%. In Figure 2, $SD - ERI_{COR} - Mie_{Scatter}$ values below the red fitting line correspond to lower ERI_{COR} values and higher absorption coefficient values measured by AE33 ($AE33_{abs-660}$) as indicated by the color and area of the markers. Higher ERI_{COR} values and low $AE33_{abs-660}$ values correspond to very high $SD - ERI_{COR} - Mie_{Scatter}$ values, in relation to the red line.

4.2. Comparison of EOLE lidar to Nephelometer and Aethalometer total ambient extinction coefficient

In order to compare in situ and remote sensing instruments, we calculated the average EOLE extinction coefficients at 355 and 532 nm for a height from 1,200 m asl to 1,300 m asl for days selected based on the procedure in section 3.9. For these days ϵ exhibited values higher than 10^{-4} for a height extending from 15 to 1,000 m agl. The comparison days included the 22nd of May 20:30 to 21:30, 23rd of May 20:30 to 21:30, 7th of June 22:00 to 23:00 and 10th of June 18:45 to 19:45. Then, we deduced the EOLE extinction AE and calculated the EOLE extinction coefficient at the wavelength of 660 nm. The in situ ambient scattering coefficient was calculated using the Nephelometer measurements, equation 2 and a γ factor equal to 0.57, corresponding to polluted marine aerosol (Gassó et al., 2000). We consider this γ factor suitable for the selected days that display high turbulence in the atmosphere, as the AMA has in general a high impact from anthropogenic activities (vehicle emissions, cooking, shipping) and it is also frequently under the influence of the sea breeze (Gini et al., 2019). We assumed that the absorption coefficient, measured by the AE33, did not change due to hygroscopic growth of particles. This assumption is plausible, as the scattering is the dominant part of the extinction as indicated by the fact that the minimum single scattering albedo (SSA) for the selected days is 0.94. SSA is the fraction in which the numerator is the scattering coefficient and the denominator the extinction coefficient. The origin of airmasses for a height up to 100 m agl calculated by FLEXPART is included as supplementary material (Figures S17-S20).

The comparison of the ambient extinction coefficient from Nephelometer and Aethalometer for ambient conditions, and the extinction coefficient obtained by EOLE for a height up to 1,300 m asl (DEM station is at 270 m asl) is presented in Figure 3a. Both extinction coefficients were adjusted to the wavelength of 660 nm. The size of the marker corresponds to the growth factor measured by the HTDMA (range: 1.004-1.21) and the color of the markers corresponds to the average ϵ value for a height extending from 15 to 1,000 m agl (range: 8×10^{-4} - 2.5×10^{-1}). The red line depicts the best linear fit obtained. We observe in Figure 3a that there is good agreement between the extinction coefficient obtained by in situ instruments to the one obtained by EOLE lidar for selected days that exhibit turbulence to heights above 1,000 m agl. The vertical distribution of the ϵ values for these days are presented as supplementary material (Figures S1-S4, depicting 22-23 of May, 7 and 10 of June). $NEPH - AETH_{EXT-WET-660}$ and $EOLE_{EXT-660}$ are well correlated (R^2 equal to 0.69 for the linear fit $NEPH - AETH_{EXT-WET-660} = 1.11 * EOLE_{EXT-660} + 23.4$ Mm^{-1}). We observe that the intercept is 23.4 Mm^{-1}, indicating that we always expect to have higher aerosol concentration at ground level, even for days that exhibit high turbulence. The RH during the lidar measurements in Figures S5-S8 (supplementary) at a height of 1,000 m agl ranged from 55% to 75%. We observe that the growth factor has little effect on the correlation of $NEPH - AETH_{EXT-WET-660}$ and $EOLE_{EXT-660}$ for the measurements presented in Figure 3a. The data point with the lowest ϵ value is the furthest one from the best linear fit (red line), indicating that the main mechanism that influences the $NEPH - AETH_{EXT-WET-660}$ and $EOLE_{EXT-660}$ correlation is the state of mixing in the vertical, while the growth factor impact appears to be small. The temporal evolution of the range-corrected lidar signal (RCS) EOLE lidar measurements at the wavelength of 1064 nm are presented as supplementary mate-

7

rial (Figures S9-S12). These vertical distribution plots indicate that the aerosol concentration during the comparison hours is almost uniform from ground level up to approximately 1,000 m asl, probably due to high turbulence in the atmosphere.

The extinction values for the $EOLE_{EXT-660}$ and $NEPH - AETH_{EXT-WET-660}$ are also presented in Table 2.

4.3. Comparison of EOLE lidar and $RI_{AE33-NEPH}$ calculated extinction coefficients

The comparison of the ambient extinction coefficient obtained by Mie algorithm calculation using $RI_{AE33-NEPH}$ retrieved from Nephelometer and Aethalometer for ambient conditions, for sizes up to 1,000 nm and the extinction coefficient obtained from EOLE for a height up to 1,300 m asl is presented in Figure 3b. Both extinction coefficients were adjusted to the wavelength of 660 nm. The size of the marker corresponds to the growth factor measured by the HTDMA (range: 1.004-1.21) and the color of the markers corresponds to the average ϵ value for a height extending from 15 to 1,000 m agl (range: 8×10^{-4} - 2.5×10^{-1}). The red line depicts the best linear fit obtained. In Figure 3b there is good agreement between the $RI_{AE33-NEPH}$ calculated extinction coefficient ($NEPH - AETH_{RI-EXT-WET-660}$) and $EOLE_{EXT-660}$ (R^2 is equal to 0.56, $NEPH - AETH_{RI-EXT-WET-660} = 0.61 *$ $EOLE_{EXT-660} + 10.2\ Mm^{-1}$) for selected days that exhibit turbulence to heights up to 1,000 m agl. We observe that the intercept is 10.2 Mm^{-1}, indicating that we always expect to have higher aerosol concentration at ground level, even for days that exhibit high turbulence. We have to keep in mind that during the deduction of $RI_{AE33-NEPH}$ the size distribution (SD) up to a maximum diameter of 1,000 nm dry diameter was used, leading to possible errors related to larger sizes of particles that were not included. We observe that the growth factor has little effect on the correlation of $NEPH - AETH_{RI-EXT-WET-660}$ and $EOLE_{EXT-660}$ for the measurements presented in Figure 3b. The data point with the lowest ϵ value is the furthest one from the best linear fit line, indicating that the main mechanism that influences the $NEPH - AETH_{RI-EXT-WET-660}$ and $EOLE_{EXT-660}$ correlation is the state of mixing in the vertical, while the growth factor impact appears to be small.

The extinction values for the $EOLE_{EXT-660}$ and $NEPH - AETH_{RI-EXT-WET-660}$ are also presented in Table 2.

### 4.4. Comparison of EOLE lidar extinction coefficient to ERI_{COR} calculated ambient scattering coefficient

The comparison of the ambient scattering coefficient obtained by Mie algorithm calculation using ERI_{COR} for ambient conditions, for sizes up to 1,000 nm, and the extinction coefficient obtained from EOLE is presented in Figure 3c. Both coefficients were adjusted to the wavelength of 660 nm. The size of the marker corresponds to the growth factor measured by the HTDMA (range: 1.004-1.21) and the color of the markers corresponds to the average ϵ value for a height extending from 15 to 1,000 m agl (range: 8×10^{-4} - 2.5×10^{-1}). The red line depicts the best linear fit obtained: $ERI_{TOTAL-SC-WET-660} = 0.62$ $* EOLE_{EXT-660} + 22\ Mm^{-1}$. We observe that the intercept is 22
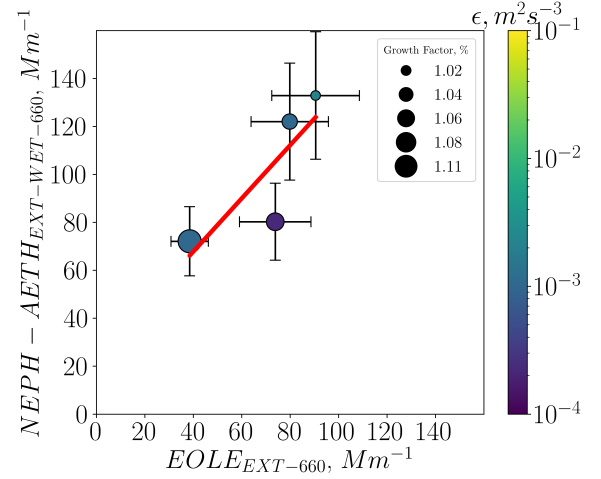
(a) $NEPH - AETH_{EXT-WET-660}$ to $EOLE_{EXT-660}$
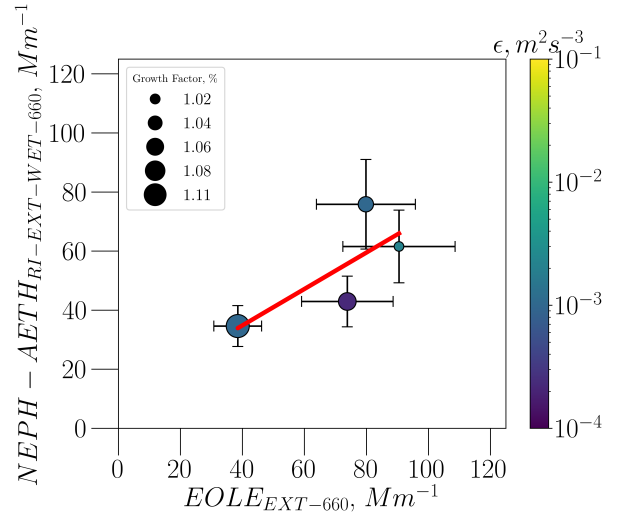
(b) $NEPH - AETH_{RI-EXT-WET-660}$ to $EOLE_{EXT-660}$
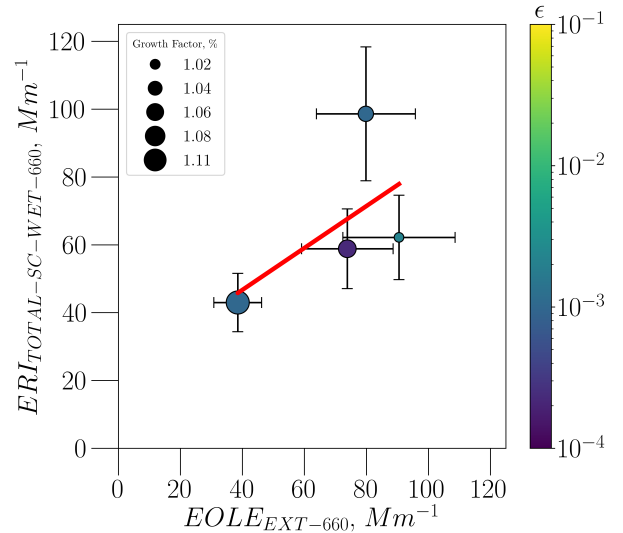
(c) $ERI_{TOTAL-SC-WET-660}$ to $EOLE_{EXT-660}$

Figure 3: In situ - Remote sensing instruments measurements comparison. Error bars correspond to 20% uncertainty.

8

Table 2: $EOLE_{EXT-660}$, $NEPH - AETH_{EXT-WET-660}$, $NEPH - AETH_{RI-EXT-WET-660}$ and $ERI_{TOTAL-SC-WET-660}$ values for the selected days.

Date, Time (UTC)	$EOLE$ $EXT-660$ Mm^{-1}	$NEPH$ $AETH$ $EXT-WET$ 660 Mm^{-1}	$NEPH$ $AETH$ $RI-EXT$ $WET-660$ Mm^{-1}	ERI $TOTAL-SC$ $WET-660$ Mm^{-1}
22nd of May 2014, 20:30-21:30	79.8	122	75.8	98.6
23rd of May 2014, 20:30-21:30	73.8	80.2	42.9	58.8
7th of June 2014, 22:00-23:00	38.5	72	34.6	43
10th of June 2014, 18:45-19:45	90.5	132.9	61.6	62.2

Mm^{-1}, indicating that we always expect to have higher aerosol concentration at ground level, even for days that exhibit high turbulence. In Figure 3c we observe that there is not satisfactory agreement between the ERI_{COR} calculated ambient scattering coefficient to the EOLE lidar extinction coefficient for selected days that exhibit turbulence to heights above 1,000 m agl (R^2 is equal to 0.35). We have to keep in mind that the absorption coefficient cannot be calculated, as ERI_{COR} corresponds to the real part of the aerosol refractive index. There is also the problem with the use of the SD up to 1,000 nm mentioned in section 3.3. Neither growth factor or ϵ appear to have a significant impact on the correlation between $ERI_{TOTAL-SC-WET-660}$ and $EOLE_{EXT-660}$. Nevertheless, as indicated in Figure 3c, ERI_{COR}, which is calculated based on the size distributions of SMPS and OPC, provides a useful insight into the optical properties of aerosols in the atmosphere not only at ground level but also at higher altitudes.

The extinction values for the $EOLE_{EXT-660}$ and the scattering values for $ERI_{TOTAL-SC-WET-660}$ are also presented in Table 2.

4.5. Comparison of EOLE lidar to Nephelometer and Aethalometer extinction AE

In Figure 4 we compare the extinction AE from EOLE and in situ measurements. The comparison is not satisfactory, as the R^2 is equal to 0.4. We have to keep in mind that the EOLE extinction AE is calculated based on measurements at 355, 532 nm, while the in situ extinction AE is calculated based on 470, 660 nm wavelength. These differences in the extinction AE indicate that the size distribution at ground level and at a height between 1,200 and 1,300 m asl are different, even though we adjusted the in situ size distribution up to a maximum diameter of 1,000 nm considering its hygroscopic growth. The AE discrepancies may be attributed to particles with aerodynamic diameter larger than 10 μm that could be present in the atmosphere but not sampled by the in situ instruments due to their PM_{10} inlet heads. We observe that the growth factor has little effect on the correlation of $NEPH-AETH_{EXT-WET-Ångstrøm}$ and $EOLE_{EXT-Ångstrøm}$ for the measurements presented in Figure 4.
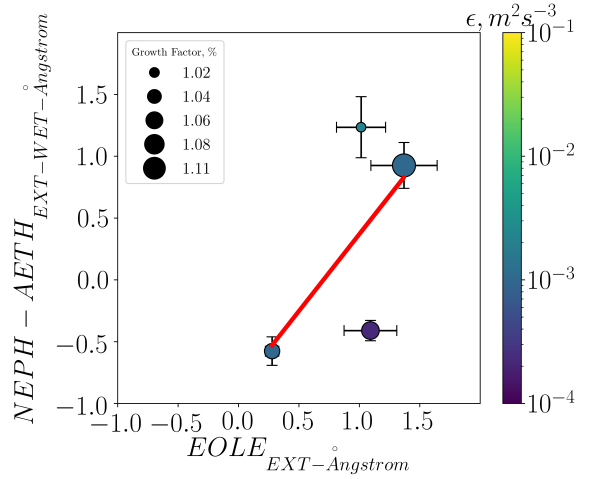

Figure 4: Comparison of the AE obtained from EOLE for the height 1,200 m to 1,300 m asl to the one acquired by in situ Nephelometer-Aethalometer measurements. The size of the marker corresponds to the growth factor measured by the HTDMA (range: 1.004-1.21) and the color of the markers corresponds to the average ϵ value for a height extending from 15 to 1,000 m agl (range: 8×10^{-4} - 2.5×10^{-1}). Both quantities are normalized between 100 and 200. Darker color corresponds to higher ϵ, while larger area corresponds to higher growth factor. The red line depicts the relation of $NEPH - AETH_{EXT-WET-Ångstrøm}$ = 1.24 * $EOLE_{EXT-Ångstrøm}$-0.88, which is the best linear fit obtained, with a coefficient of determination (R^2) equal to 0.4. Error bars correspond to 20% uncertainty.

The data point with the lowest ϵ value is the one furthest from the red best fit line, indicating that the main mechanism that influences the $NEPH - AETH_{EXT-WET-660}$ and $EOLE_{EXT-660}$ correlation is the state of mixing in the vertical.

The values for the $EOLE_{EXT-Ångstrøm}$ and $NEPH - AETH_{EXT-WET-Ångstrøm}$ are also presented in Table 3. We observe that on the 22nd of May 2014 the $EOLE_{EXT-Ångstrøm}$ and $NEPH - AETH_{EXT-WET-Ångstrøm}$ values are below 1. This indicates Saharan dust aerosol (coarse mode aerosol in general). The fact that at ground level the Ångstrøm exponent is lower, could indicate higher content of large aerosol particles (approximating PM_{10}) due to their higher stokes terminal velocity.

Table 3: $EOLE_{EXT-Ångstrøm}$ and $NEPH - AETH_{EXT-WET-Ångstrøm}$ values for the selected days.

Date, Time (UTC)	$EOLE_{EXT}$ Ångstrøm	$NEPH - AETH_{EXT-WET}$ Ångstrøm
22nd of May 2014, 20:30-21:30	0.28	-0.58
23rd of May 2014, 20:30-21:30	1.09	-0.41
7th of June 2014, 22:00-23:00	1.37	0.92
10th of June 2014, 18:45-19:45	1.01	1.23

9

4.6. Mixing of local and regional aerosol on the 27th of May 2014

The $PM_{2.5}$ concentration of mineral dust on a 24-h filter at DEM station on the 27th of May was 3.5 $\mu g m^{-3}$. The estimation is based on XRF measurements and equation 5. This day is presented as an example of the information we acquire by the synergy of remote sensing and in situ instruments regarding the mechanism that allows the mixing in the vertical of long range transported and locally produced aerosol. This mechanism is very important as it will allow us to predict the dispersion of aerosol and subsequently, using lung deposition models, its impact on the health and quality of life of the people living in the AMA.

In Figure 5a (EOLE range-corrected signal (A.U.) at 1064 nm), a Saharan dust layer is present above 1,500 m asl (06:00-09:00 UTC) and a local pollution layer is present at lower altitudes. At 12:00 UTC (due to intense turbulence in the atmosphere as indicated in Figure 6a), the two layers are mixing. In the afternoon, a well mixed layer (local pollution and Saharan dust) is present up to 2,000 asl (Figure 5a). This is also indicated in Figure 5c, where the AE for the averaged period 11:30-12:30 UTC and for the height between 1,800 and 2,500 m asl is below 1, while for the averaged period 19:30-20:30 UTC the Saharan dust layer has descended to heights below 1,300 m asl, as the AE $AE_{b-355/532}$ is above 1 for all altitudes depicted. Please note that the $AE_{b-355/532}$ could not be determined for heights below 1300 m asl for the averaged period 19:30-20:30 UTC. Figure 6a displays the ϵ values on the 27th of May. From 09:00 UTC until almost the end of the day, there is turbulence in the atmosphere up to the height of 1,000 m agl (approximately 1,300 m asl). In Figure 6b, after 12:00, the aerosol scattering coefficient values measured at ground level (wavelength of 470 and 660 nm) are getting very close to each other (AE is decreasing, an indication of Saharan dust, (Coen et al., 2004)). At 18:00, the Saharan dust dominates the aerosol concentration at ground level as the scattering coefficient at 660 nm is higher than that at 470 nm. Figure 6c demonstrates that air masses reaching DEM station have a significant residence time in a height up to 100 m agl (very close to the ground) in North Africa. As indicated by the residence time color plot, the air masses from North Africa are partly lifted to altitudes higher than 100 m agl and subsequently they move downwards to DEM station, depositing Saharan dust. Figure S13 (supplementary material) presents a radiosonde measurement at 12:00 UTC. It demonstrates a region of low RH, which is consistent with a Saharan dust layer, mainly between 1,000 and 2,000 m agl.

In an earlier study, Diapouli et al. (2017b) reported for DEM station a mean annual concentration for African dust of 1.49 and 4.19 $\mu g m^{-3}$ for $PM_{2.5}$ and PM_{10} size fractions, respectively. Keeping in mind that on the 27th of May 2014, the mixing process of Sahara dust and local urban polluted aerosol starts after 12:00 UTC, the $PM_{2.5}$ mineral dust concentration collected on a 24-h filter should be at least doubled to represent the conditions at DEM station in the late afternoon. Thus we conclude that the dust concentration on this day is significantly higher than the background dust concentration and the impact of transported aerosol is significant.

In the AMA Sahara dust events are frequent, therefore the example day presented is very useful, as it promotes knowledge on the mechanism by which dust particles intensify pollution (Soupiona et al., 2018). This knowledge can be integrated in models that predict the impact of aerosol particles to human health. Thus, using a combination of in situ instruments, remote sensing instruments and models, we could increase the quality of life for people living in the AMA.

5. Summary and Conclusions

In this study, aerosol in situ and remote sensing instruments measurements, conducted in the Athens Metropolitan area during the summer of 2014, were combined either by comparison or by complementary use.

We found that within the systematic uncertainties associated with each instrument described, comparison between in situ and remote sensing instruments is possible for collocated in situ and remote sensing stations, even when the sampled volume is not the same (in situ measurements take place at ground level, while the lidar measurement volume is at a height of several hundred meters agl).

A method was developed in order to assure that the comparison is feasible, yielding satisfactory results. This was based on choosing conditions where a well mixed boundary layer up to 1,300 m can be documented.
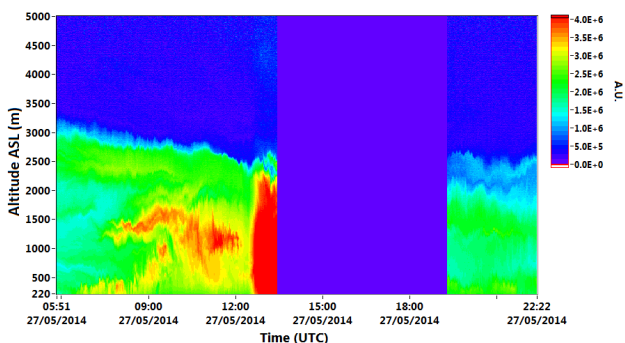
In an effort to acquire the fraction of the in situ measured size distribution that could be used in order to compare in situ and remote sensing instruments, we compared the dry Nephelometer scattering coefficient and ERI_{COR} calculated scattering coefficient. We concluded that the size distribution acquired by SMPS and OPC up to a maximum diameter of 1,000 nm (electrical mobility diameter) is a good choice so as to calculate, using Mie algorithm, the optical properties of the aerosol volume sampled by in situ instruments.

The ambient aerosol extinction coefficient calculated from in situ scattering and absorption coefficients is compared to the EOLE extinction coefficient and good agreement is observed between the two quantities, indicating that Nephelometer and Aethalometer can provide aerosol optical properties representative of the common MH volume.
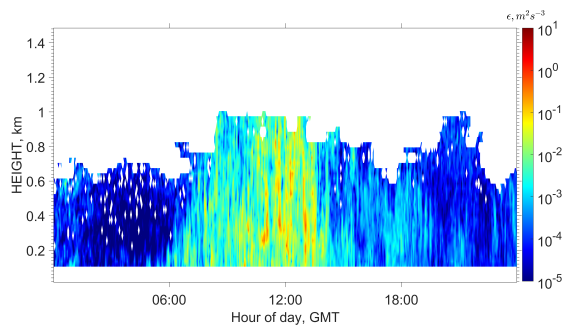
When the in situ extinction coefficient is calculated by the derived in situ size distribution and the derived $RI_{AE33-NEPH}$ (by the optical properties data) and then compared to the derived EOLE lidar extinction coefficient, good agreement between in situ and remote sensing data is observed.

The EOLE lidar extinction coefficient to ERI_{COR} calculated ambient scattering coefficient are not in good agreement, but we have to keep in mind that ERI_{COR} corresponds to the real part of the refractive index. Still, we have a useful result for days with high turbulence in the atmosphere, even for higher altitudes.
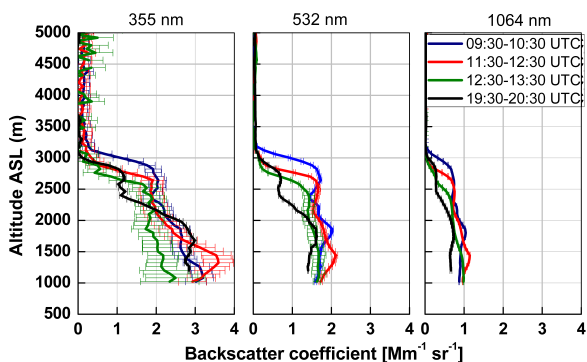
The agreement between the Nephelometer and Aethalometer calculated extinction AE and the one calculated by EOLE lidar is rather poor, and this probably displays that the size distributions measured by in situ and remote sensing instruments
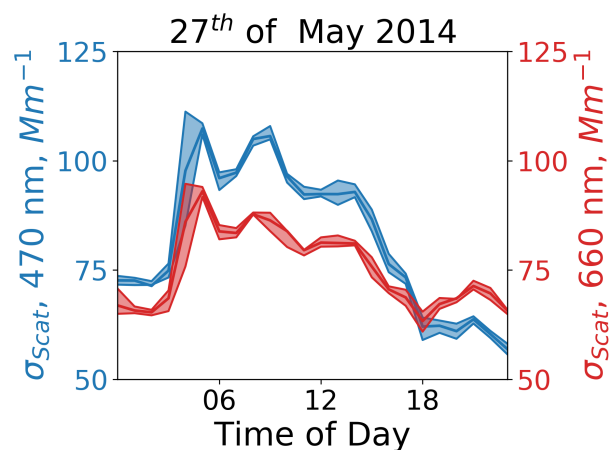
(a) Temporal evolution of the range-corrected lidar signal (RCS) at 1064 nm observed by EOLE, in arbitrary units (A.U.)
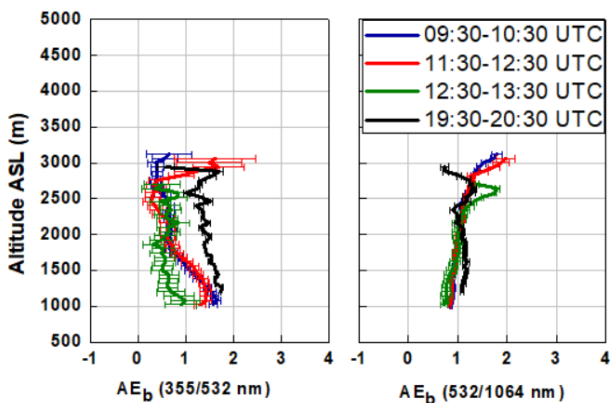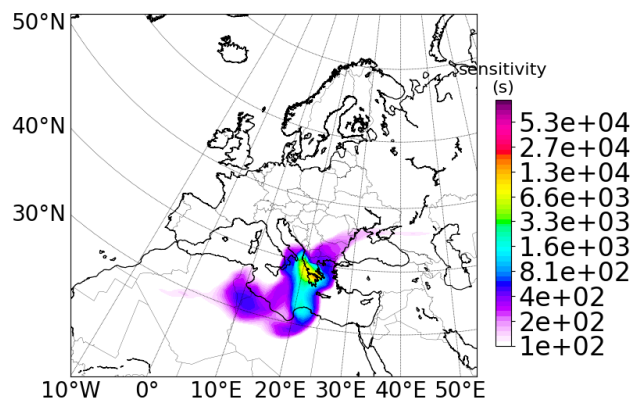

(b) EOLE backscatter lidar signals at 355, 532 and 1064 nm.

(c) EOLE *AE*.

Figure 5: Subfigure a: Temporal evolution of the range-corrected lidar signal (RCS) at 1064 nm observed by EOLE, in arbitrary units (A.U.). Until 09:00 UTC a Saharan dust layer is present above 1,500 m asl and a local pollution layer at ground level. At 12:00, due to strong turbulence up to 1,000 m, the two layers are mixing. In the afternoon, a well mixed layer up to 2,000 asl has developed. This is also demonstrated in subfigure c, where the *AE* at 11:30 to 12:30 indicates that a Saharan dust layer is present at 1,800 to 2,500 m asl (Ångström below 1), but at 19:30 to 20:30 the Saharan dust layer is missing, indicating that it has descended to lower altitudes. Subfigure b: EOLE backscatter lidar signals at 355, 532 and 1064 nm. Subfigure c: EOLE *AE*.

(a) ϵ vertical distribution.

(b) Nephelometer scattering coefficient, 470-660 nm.

(c) Air mass origin from a height up to 100 m agl.

Figure 6: Subfigure (a) displays the ϵ values during the 27th of May. From 09:00 UTC until almost the end of the day, there is turbulence in the atmosphere up to the height of 1,000 m agl. Subfigure b: After 12:00, the aerosol scattering coefficient values measured at ground level (470 and 660 nm) are getting very close (*AE* is decreasing, an indication of Saharan dust) and finally at 18:00, the Saharan dust layer is at ground level dominating particle concentration, as the scattering coefficient at 660 nm is higher than that at 470 nm. Subfigure (c) indicates that air masses with significant residence time over North Africa from a height up to 100 m agl reach DEM station on the 27th of May at 18:00-21:00.

have differences that lead to different *AE*s. This could be partly attributed to particles with aerodynamic diameter larger than 10 μm present in the atmosphere but not sampled by the in situ instruments due to their PM_{10} inlet heads and partly to the higher uncertainty in the EOLE extinction AE measurement, up to 25%.

Finally, we demonstrate the results that can be obtained by the synergy of in situ and remote sensing instruments. Thus, we obtain an insight on how regional aerosol is added to local aerosol, especially during pollution events due to long range transport.

Further work on the subject should include longer periods of parallel in situ - remote sensing measurement campaigns in collocated stations. We could also include the comparison of high altitude in situ station measurements to remote sensing instrument measurements placed at a lower altitude (all instruments measuring the same air volume). Thus we will be able to study in more detail aerosol physico-chemical properties, aerosol-cloud interactions, cloud micro-physics, and Condensation Cloud Nuclei formation.

Argyrouli, A., Sep. 2016. Study of the planetary boundary layer & its influence on cloud properties. Ph.D. thesis, School of Applied Mathematics & Physical Sciences, National Technical University of Athens.

Bezantakos, S., Barmpounis, K., Giamarelou, M., Bossioli, E., Tombrou, M., Mihalopoulos, N., Eleftheriadis, K., Kalogiros, J., Allan, J. D., Bacak, A., Percival, C. J., Coe, H., Biskos, G., 2013. Chemical composition and hygroscopic properties of aerosol particles over the Aegean Sea. Atmos. Chem. Phys. 13, 11595–11608.

Bohren, C., Huffman, D. R., 1998. Absorption and Scattering of Light by Small Particles. Wiley Science Paperback Series.

Bryant, C., Eleftheriadis, K., Smolík, J., Zdimal, V., Mihalopoulos, N., Colbeck, I., 2006. Optical properties of aerosols over the eastern Mediterranean. Atmospheric Environment 40 (32), 6229–6244.

Bukowiecki, N., Zieger, P., Weingartner, E., Juranyi, Z., Gysel, M., Neininger, B., SCHNEIDER, B., Hueglin, C., Ulrich, A., Wichser, A., Henne, S., Brunner, D., Kaegi, R., Schwikowski, M., Tobler, L., Wienhold, F. G., Engel, I., Buchmann, B., Peter, T., Baltensperger, U., 2011. Ground-based and airborne in-situ measurements of the Eyjafjallaj okull volcanic aerosol plume in Switzerland in spring 2010. Atmos. Chem. Phys. 11, 10011–10030.

Coen, M., Weingartner, E., Schaub, D., Hueglin, C., Corrigan, C., Henning, S., Schwikowski, M., Baltensperger, U., Dec. 2004. Saharan dust events at the Jungfraujoch: detection by wavelength dependence of the single scattering albedo and first climatology analysis. Atmos. Chem. Phys. 4, 2465–2480.

Crewell, S., Czekala, H., Lohnert, U., Simmer, C., Rose, T., Zimmermann, R., 2001. Micro- wave radiometer for cloud cartography: a 22-channel ground-based microwave radi- ometer for atmospheric research. Radio Sci. 36 (4), 621–638.

Diapouli, E., Manousakas, M., Vratolis, S., Vasilatou, V., Maggos, T., Saraga, D., Grigoratos, T., Argyropoulos, G., Voutsa, D., Samara, C., Eleftheriadis, K., 2017a. Evolution of air pollution source contributions over one decade, derived by PM 10 and PM 2.5 source apportionment in two metropolitan urban areas in Greece. Atmos. Environ. 164, 416–430.

Diapouli, E., Manousakas, M. I., Vratolis, S., Vasilatou, V., Pateraki, S., Bairachtari, K. A., Querol, X., Amato, F., Alastuey, A., Karanasiou, A. A., Lucarelli, F., Nava, S., Calzolai, G., Gianelle, V. L., Colombi, C., Alves, C., Custódio, D., Pio, C., Spyrou, C., Kallos, G. B., Eleftheriadis, K., 2017b. AIRUSE-LIFE + : estimation of natural source contributions to urban ambient air PM_{10} and $PM_{2.5}$ concentrations in southern Europe – implications to compliance with limit values. Atmos. Chem. Phys., 17, 3673–3685.

Flocas, H. A., Helmis, C. G., Blikas, S. N., Asimakopoulos, D. N., Bartzis, J. G., Deligiorgi, D. G., 1998. Mean Characteristics of the Katabatic Flow of a 1024 m High Knife Edge Mountain. Theor. Appl. Climatol. 59, 237–249.

Fuzzi, S., Baltensperger, U., Carslaw, K., Decesari, S., Denier van der Gon, H., Facchini, M. C., Fowler, D., Koren, I., Langford, B., Lohmann, U., Nemitz, E., Pandis, S., Riipinen, I., Rudich, Y., Schaap, M., Slowik, J. G., Spracklen, D. V., Vignati, E., Wild, M., Williams, M., Gilardoni, S., 2015. Particulate matter, air quality and climate: lessons learned and future needs. Atmos. Chem. Phys. 15, 8217–8299.

Gassó, S., Hegg, D. A., Covert, D. S., Collins, D., Noone, K. J., Öström, E., Schmid, B., Russell, P. B., Livingston, J. M., Durkee, P. A., Jonsson, Å. M., 2000. Influence of humidity on the aerosol scattering coefficient and its effect on the upwelling radiance during ACE-2. Tellus B: Chemical and Physical Meteorology 52 (2), 546–567.

Gini, M., Diapouli, E., Vratolis, S., Helmis, C., Eleftheriadis, K., 2019. Microphysical and selected chemical properties of ambient aerosol at a suburban environment with emphasis on the size resolved Fuchs surface area and air circulation patterns . In preparation.

Google, 2019. Google Map of Attica.

Grimm-Aerosoltechnik, 2005. Portable Dust Monitor SERIES 1.100.

Hasan, H., Dzubay, T. G., 1983. Apportioning light extinction coefficients chemical species in atmospheric aerosol. Atmos. Environ. 17 (8), 1573–1581.

Heim, M., Mullins, B. J., Umhauer, H., Kasper, G., 2008. Effects of Mixing on Extinction by Carbonaceous Particles. J. Aerosol Sci 39, 1019–1031.

Kalogridis, A.-C., Vratolis, S., Liakakou, E., Gerasopoulos, E., Mihalopoulos, N., Eleftheriadis, K., 2018. Assessment of wood burning versus fossil fuel contribution to wintertime black carbon and carbon monoxide concentrations in Athens, Greece. Atmos. Chem. Phys. 18, 10219–10236.

Kokkalis, P., Papayannis, A., Mamouri, R., Tsaknakis, G., Amiridis, V., 2012. The EOLE lidar system of the National Technical University of Athens. Proc. 26th International Laser Radar Conference (26th ILRC), Porto Heli, Greece, 629–632.

Labzovskii, L. D., Papayannis, A., Binietoglou, I., Banks, R. F., Baldasano, J. M., Toanca, F., Tzanis, C. G., Christodoulakis, J., 2018. Relative humidity vertical profiling using lidar-based synergistic methods in the framework of the Hygra-CD campaign. Ann. Geophys. 36, 213–229.

Lazaridis, M., Eleftheriadis, K., Smolík, J., Colbeck, I., Kallos, G., Drossinos, Y., Zdimal, V., Vecera, Z., Mihalopoulos, N., Mikuška, P., Bryant, C., Housiadas, C., Spyridaki, A., Astitha, M., Havranek, V., 2006. Dynamics of fine particles and photo-oxidants in the Eastern Mediterranean (SUB-AERO). Atmospheric Environment 40 (32), 6214–6228.

Liljegren, J. C., Boukabara, S.-A., Cady-Pereira, K., Clough, S., 2005. The effect of the half- width of the 22-GHz water vapour line on retrievals of temperature and water va- pour profiles with a 12-channel microwave radiometer. IEEE Trans. Geosci. Remote Sens. 43 (5), 1102–1108.

Loehnert, U., Crewell, S., 2003. Accuracy of cloud liquid water path from ground-based microwave radiometry. Radio Sci. 38 (3), 8042.

Lymperopoulos, Y., 2015. Personal communication. Grimm Aerosoltechnik.

Mamouri, R., Papayannis, A., Tsaknakis, G., Amiridis, V., 2007. Six-month ground-based water vapour Raman lidar measurements over Athens, Greece and system validation. J. Optoel. Adv. Materials 9, 3546–3549.

Manousakas, M., Diapouli, E., Papaefthymiou, H., Kantarelou, V., Zarkadas, C., Kalogridis, A.-C., A.-G., K., Eleftheriadis, K., 2017. XRF characterization and source apportionment of PM10 samples collected in a coastal city. X-Ray Spectrometry, 1–11.

Maroufidis, J., Mylonaki, M., Soupiona, O., Papayannis, A., 2020. Detection and Segmentation of Aerosol Layers & Clouds in Atmospheric Lidar Mea-

surements. Atmospheric Environment In preparation.

Müller, T., Laborde, M., Kassell, G., Wiedensohler, A., 2011. Design and performance of a three-wavelength LED-based total scatter and backscatter integrating nephelometer . Atmos. Meas. Tech. 4, 1291–1303.

Nash, J., Oakley, T., Vömel, H., Wei, L., 2011. WMO intercomparison of high quality radio- sonde systems, Yangjiang, China, 12 July–3 August 2010. World Meteorological Organization Instruments and Observing Methods, Report No. 107.

Nava, S., Becagli, S., Calzolai, G., Chiari, M., Lucarelli, F., Prati, P., Traversi, R., Udisti, R., Valli, G., Vecchi, R., 2012. Saharan dust impact in central Italy: An overview on three years elemental data records. Atmos. Environ. 60, 444–452.

O'Connor, E., Illingworth, A., Brooks, I., Westbrook, C., Hogan, R., Davies, F., Brooks, B., 2010. A Method for Estimating the Turbulent Kinetic Energy Dissipation Rate from a Vertically Pointing Doppler Lidar, and Independent Evaluation from Balloon-Borne In Situ Measurements. JOURNAL OF ATMOSPHERIC AND OCEANIC TECHNOLOGY 27, 1652–1664.

Pandolfi, M., Alados-Arboledas, L., Alastuey, A., Andrade, M., Artiñano, B., Backman, J., Baltensperger, U., Bonasoni, P., Bukowiecki, N., Collaud Coen, M., Conil, S., Coz, E., Crenn, V., Dudoitis, V., Ealo, M., Eleftheriadis, K., Favez, O., Fetfatzis, P., Fiebig, M., Flentje, H., Ginot, P., Gysel, M., Henzing, B., Hoffer, A., Holubova Smejkalova, A., Kalapov, I., Kalivitis, N., Kouvarakis, G., Kristensson, A., Kulmala, M., Lihavainen, H., Lunder, C., Luoma, K., Lyamani, H., Marinoni, A., Mihalopoulos, N., Moerman, M., Nicolas, J., O'Dowd, C., Petäjä, T., Petit, J.-E., Pichon, J. M., Prokopciuk, N., Putaud, J.-P., Rodríguez, S., Sciare, J., Sellegri, K., Stamenov, D. B., Swietlicki, E., Titos, G., Tuch, T., Tunved, P., Ulevicius, V., Vaishya, A., Vana, M., Virkkula, A., Vratolis, S., Weingartner, E., Wiedensohler, A., Laj, P., 2018. A European aerosol phenomenology-6: Scattering properties of atmospheric aerosol particles from 28 ACTRIS sites. Atmos. Chem. Phys. 18, 7877–7911.

Papayannis, A., Argyrouli, A., Bougiatioti, A., Remoundaki, E., Vratolis, S., Nenes, A., Solomos, S., Komppula, M., Giannakaki, E., Kalogiros, J. A., Banks, R. F., Eleftheriadis, K., Mantas, E., Diapouli, E., Tzanis, C. G., Kazadzis, S. A., Binietoglou, I., Labzovskiǐ, L., Vande Hey, J. D., Zerefos, C. S., 2017. An overview from hygroscopic aerosols to cloud droplets: The HygrA-CD campaign in the Athens basin . Sci. Total Environ. 574, 216–233.

Sawamura, P., Moore, R. H., Burton, S. P., Chemyakin, E., Müller, D., Kolgotin, A., Ferrare, R. A., Hostetler, C. A., Ziemba, L. D., Beyersdorf, A. J., Anderson, B. E., 2017. HSRL-2 aerosol optical measurements and microphysical retrievals vs. airborne in situ measurements during DISCOVER-AQ 2013: an intercomparison study. Atmos. Chem. Phys. 17, 7229–7243.

Schneider, F., 2016. Personal communication.

Skamarock, W. C., Klemp, J. B., Dudhia, J., Gill, D. O., Barker, D. M., Wang, W., Powers, J. G., 2005. A Description of theAdvanced Research WRF Version 2. NCAR Tech. Note NCAR/TN-468+STR.

Solomos, S., Bougiatioti, A., Soupiona, O., Papayannis, A., Mylonaki, M., Papanikolaou, C., Argyrouli, A., Nenes, A., 2019. Effects of regional and local atmospheric dynamics on the aerosol and CCN load over Athens. Atmos. Environ. 197, 53–65.

Soupiona, O., Papayannis, A., Kokkalis, P., Mylonaki, M., Tsaknakis, G., Argyrouli, A., Vratolis, S., Jun. 2018. Long-term systematic profiling of dust aerosol optical properties using the EOLE NTUA lidar system over Athens, Greece (2000-2016). Atmos. Environ. 183, 165–174.

Stelson, A. W., 1990. Urban Aerosol Refractive Index Prediction by Partial Molar Refraction Approach. Environ. Sci. Technol. 24, 1676–1679.

Stohl, A., Forster, C., Frank, A., Seibert, P., Wotawa, G., 2005. Technical Note: The Lagrangian particle dispersion model FLEXPART version 6.2. Atmos. Chem. Phys 5, 2461–2474.

Stohl, A., Thomson, D. J., 1999. A density correction for Lagrangian particle dispersion models. Bound.-Layer Met. 90, 155–167.

Stolzenburg, M. R., McMurry, P. H., 1991. An Ultrafine Aerosol Condensation Nucleus Counter. Aerosol Science and Technology 14, 48–65.

Tucker, S., Brewer, A. W., Banta, R. M., Senff, C. J., Sandberg, P., C., L. D., Weickmann, A. M., Hardesty, M. R., 2009. Doppler Lidar Estimation of Mixing Height Using Turbulence, Shear, and Aerosol Profiles. JOURNAL OF ATMOSPHERIC AND OCEANIC TECHNOLOGY 26, 673–688.

Vaisala, 2013a. Vaisala radiosonde RS92 performance in the WMO intercomparison of high quality radiosonde systems, Yangjiang, China 2010. Vaisala White Paper May 2013, Ref. B211129EN-D.

Vaisala, 2013b. Vaisala radiosonde RS92-SGP datasheet, ref. B210358EN-F.

Vratolis, S., Fetfatzis, P., Argyrouli, A., Papayannis, A., Muller, D., Veselovskii, I., Bougiatioti, A., Nenes, A., Remoundaki, E., Diapouli, E., Manousakas, M., Mylonaki, M., Eleftheriadis, K., 2018. A new method to retrieve the real part of the equivalent refractive index of atmospheric aerosols. Journal of Aerosol Science 117, 54–62.

Vratolis, S., Gini, M., Bezantakos, S., Stavroulas, I., Kalivitis, N., Kostenidou, E., Louvaris, E., Siakavaras, D., Biskos, G., Mihalopoulos, N., Pandis, S. N., Pilinis, C., Papayannis, A., Eleftheriadis, K., 2019. Particle number size distribution statistics at City-Centre Urban Background, Urban Background, and Remote stations in Greece during summer. Atmos. Environ. 213, 711–726.

Wang, L., Stanič, S., Bergant, K., Eichinger, W., Močnik, G., Drinovec, L., Vaupotič, J., Miler, M., Gosar, M., Gregorič, A., 2019. Retrieval of Vertical Mass Concentration Distributions—Vipava Valley Case Study. Remote Sensing 11 (106).

Weitkamp, C., 2005. Lidar Range-Resolved Optical Remote Sensing of the Atmosphere. Vol. 102. Springer-Verlag New York.

Wiedensohler, A., Birmili, W., Nowak, A., Sonntag, A., Weinhold, K., Merkel, M., Tuch, B. W. T., Pfeifer, S., Fiebig, M., Fjäraa, A. M., Asmi, E., Sellegri, K., Depuy, R., Venzac, H., Villani, P., Laj, P., Aalto, P., Ogren, J. A., Swietlicki, E., Williams, P., Roldin, P., Quincey, P., Hüglin, C., Fierz-Schmidhauser, R., Gysel, M., Weingartner, E., Riccobono, F., Santos, S., Grüning, C., Faloon, K., Beddows, D., Harrison, R., Monahan, C., Jennings, S. G., O'Dowd, C. D., Marinoni, A., Horn, H.-G., Keck, L., Jiang, J., Scheckman, J., McMurry, P. H., Deng, Z., Zhao, S., Moerman, M., Henzing, B., de Leeuw, G., Löschau, G., Bastian, S., 2012. Mobility particle size spectrometers: harmonization of technical standards and data structure to facilitate high quality long-term observations of atmospheric particle number size distributions. Atmos. Meas. Tech. 5, 657–685.

Zhang, Y., Gao, Z., Li, D., Li, Y., Zhang, N., Zhao, X., Chen, J., 2014. On the computation of planetary boundary-layer height using the bulk Richardson number method. Geosci. Model Dev. 7.

Zieger, P., Kienast-Sjögren, E., Starace, M., von Bismarck, J., Bukowiecki, N., Baltensperger, U., Wienhold, F. G., Peter, T., Ruhtz, T., Coen, M. C., Vuilleumier, L., Maier, O., Emili, E., Popp, C., Weingartner, E., 2012. Spatial variation of aerosol optical properties around the high-alpine site Jungfraujoch (3580 m a.s.l.). Atmos. Chem. Phys. 12, 7231–7249.

Zieger, P., Weingartner, E., Henzing, B., Moerman, M., Leeuw, G. d., Mikkilä, J., Ehn, M., Petäjä, T., Clémer, K., van Roozendael, M., Yilmaz, S., Frieß, U., Irie, H., Wagner, T., Shaiganfar, R., Beirle, S., Apituley, A., Wilson, K., Baltensperger, U., 2011. Comparison of ambient aerosol extinction coefficients obtained from in-situ, MAX-DOAS and LIDAR measurements at Cabauw. Atmos. Chem. Phys. 11, 2603–2624.

13